

A statistical reconstruction algorithm for positronium lifetime imaging using time-of-flight positron emission tomography

Hsin-Hsiung Huang, Zheyuan Zhu, Slun Boopasiri, Zhuo Chen, Shuo Pang, and Chien-Min Kao

Abstract—Positron emission tomography (PET) is an important modality for diagnosing diseases such as cancer and Alzheimer’s disease, capable of revealing the uptake of radiolabeled molecules that target specific pathological markers of the diseases. Recently, positronium lifetime imaging (PLI) that adds to traditional PET the ability to explore properties of the tissue microenvironment beyond tracer uptake has been demonstrated with time-of-flight (TOF) PET and the use of non-pure positron emitters. However, achieving accurate reconstruction of lifetime images from data acquired by systems having a finite TOF resolution still presents a challenge. This paper focuses on the two-dimensional PLI, introducing a maximum likelihood estimation (MLE) method that employs an exponentially modified Gaussian (EMG) probability distribution that describes the positronium lifetime data produced by TOF PET. We evaluate the performance of our EMG-based MLE method against approaches using exponential likelihood functions and penalized surrogate methods. Results from computer-simulated data reveal that the proposed EMG-MLE method can yield quantitatively accurate lifetime images. We also demonstrate that the proposed MLE formulation can be extended to handle PLI data containing multiple positron populations.

Index Terms—Positron emission tomography, time-of-flight, positronium lifetime imaging, maximum likelihood.

I. INTRODUCTION

Positronium lifetime imaging (PLI) with time-of-flight (TOF) positron emission tomography (PET) represents a recent advancement in medical imaging, with its feasibility substantiated through various experimental studies [1]–[5]. Traditional PET is known for assessing the functional state of organs or tissues through the uptake of specific PET molecules. In contrast, PLI aims to measure the lifetime of positronium that is a meta-stable electron-positron pair formed by the positrons emitted by PET molecules [6]. More precisely, it measures the lifetime of so-called ortho-positronium (o-P) that can be significantly affected by the interaction of an o-P with nearby molecules, such as oxygen, that possess an unpaired electron. As a result, o-P lifetime may serve as a quantitative marker of such molecule presences in the tissue microenvironment, independent of the traditional PET molecule uptake mechanisms. This capability can be significant in clinical contexts.

This work did not involve human subjects or animals in its research.

This work was partially supported by NSF grant DMS-1924792 (Huang), DMS-2318925 (Huang) and NIH grant R01-EB029948 (Kao). Corresponding author: Hsin-Hsiung Huang.

Z. Zhu and S. Pang are with CREOL, The College of Optics and Photonics, University of Central Florida, Orlando, FL 32816 (e-mails: zyzhu@knights.ucf.edu, pang@ucf.edu)

C.-M. Kao is with Department of Radiology, University of Chicago, Chicago, IL 60637 (e-mail: ckao95@uchicago.edu).

Z. Chen is with Department of Mathematics, University of Arizona, Tucson, AZ 85721 (e-mail: zchen1@math.arizona.edu).

S. Boopasiri (email: slun.boopasiri@ucf.edu) and H.-H. Huang are with Department of Statistics and Data Science, University of Central Florida, Orlando, FL 32816 (email: hsin.huang@ucf.edu)

For instance, it may be used to identify hypoxic tissues that are often resistant to therapies [4], [7], potentially enabling enhanced treatment strategies for conditions like cancer.

Today’s TOF-PET systems have a coincidence resolving time (CRT) ranging from 200 to 600 ps full width at half maximum (FWHM) [8]–[10], corresponding to a spatial uncertainty of 3-9 cm. Consequently, the measurement can include a mixture of events originating from different locations with varying lifetimes. Initial experimental implementations of PLI address this issue by placing samples sufficiently apart relative to the system’s TOF resolution [11], [12]. However, in practical applications, such spatial separation is often not feasible.

The inverse Laplace transform method [13] has been proposed to separate various components in a lifetime histogram. This method significantly reduces information loss by accurately decomposing overlapping lifetime signals, which is a common issue with traditional averaging techniques. Unlike conventional methods that average lifetime data and obscure fine details, the inverse Laplace transform method preserves the distinct lifetime components, leading to a more precise and detailed analysis of the data. However, it does not perform image reconstruction. Several image reconstruction methods for PLI with TOF-PET have been recently reported [14]–[18]. Qi and Huang [14] developed a penalized surrogate (PS) method to produce a regularized maximum likelihood (ML) solution. Their model is based on a single-exponential probabilistic model for the PLI data, which does not account for the effects of finite CRT on the lifetime measurement. This paper introduces an extended statistical model for 2-dimensional TOF-PET PLI data that allows the lifetime distribution to contain multiple components and considers the exponentially-modified Gaussian distribution for each component to account for the uncertainty in time measurement. The ML solution according to the model was solved using the Limited-memory Broyden-Fletcher-Goldfarb-Shanno Bound (L-BFGS-B) method from `scipy.optimize` [19], imposing nonnegativity condition for the solution.

The remainder of this paper is organized as follows: Section II details the formulation of the statistical model for the PLI list-mode data and the derivation of an algorithm to obtain the maximum likelihood estimates of lifetime images. Section III describes the computer-simulation study and presents the results. Section IV offers a summary and conclusions.

II. STATISTICAL MODEL FOR TOF-PET PLI DATA

A. Detection of a PLI event with TOF-PET

Fig. 1 illustrates a two-dimensional (2D) TOF-PET system comprising a ring of uniformly spaced detectors that are

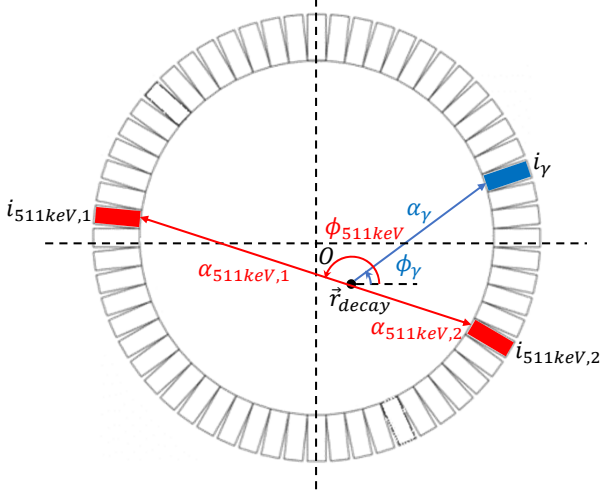


Fig. 1: Detection of a PLI event using a 2D TOF-PET system.

numerically labeled by an integer i . It is assumed that a non-pure positron-emitter such as Sc-44, which emits a positron and a gamma ray effectively at the same time (called a prompt gamma), is employed. Compared to the popular PET isotopes like F-18, many non-pure positron-emitters have a larger positron range¹ that can limit the resulting image resolution [21]–[23]. In this work, we shall neglect the positron range for it does not affect the fundamental validity of the proposed reconstruction method [14]. Similarly, photon acolinearity is also neglected [24].

The decay of an isotope like Sc-44 releases a prompt gamma and a positron at location \mathbf{r}_{decay} and time t_{decay} . As illustrated in Fig. 1, the prompt gamma travels a distance α_γ towards the detector ring at angle ϕ_γ , captured by detector i_γ at time $t_\gamma = t_{decay} + \alpha_\gamma/v_c$ where v_c is the speed of light. The positron can momentarily form a positronium before it annihilates with an electron. The elapse time before annihilation τ is described by an exponential distribution [11], given by

$$p(\tau; \lambda) = \text{Exp}(\tau; \lambda) = \begin{cases} \lambda e^{-\lambda\tau} & \tau \geq 0 \\ 0 & \tau < 0. \end{cases} \quad (1)$$

Lifetime refers to the inverse of the rate constant λ ; these two terms will be used interchangeably in this paper. There are, in fact, two positronium populations: para-positronium (p-P) and ortho-positronium (o-P). Positrons that do not form positroniums before annihilation, called direct annihilation (DA), also can exist for a finite time. The DA and p-P lifetimes are substantially shorter than the o-P lifetime. Unlike the o-P lifetime, the DA and p-P lifetimes, and the proportions of the DA, p-P and o-P populations, are not sensitive to the environment. Therefore, the main interest in PLI is the o-P lifetimes. Please see [4], [11] for in-depth discussion.

On annihilation, as depicted by the red line in the Fig. 1, two opposite 511 keV gamma rays are created. They travel from \mathbf{r}_{decay} at a random angle ϕ_{511keV} with respect to ϕ_γ and are detected by detectors $i_{511keV,1}$ and $i_{511keV,2}$ at time $t_{511keV,1} = t_{decay} + \tau + \alpha_{511keV,1}/v_c$ and $t_{511keV,2} = t_{decay} + \tau + \alpha_{511keV,2}/v_c$

respectively, where $\alpha_{511keV,1}$ and $\alpha_{511keV,2}$ are the distances that they travel.

The conventional TOF-PET system reports $i_{511keV,1}$, $i_{511keV,2}$, and the TOF given by

$$\Delta t_{511keV} = t_{511keV,1} - t_{511keV,2} = (\alpha_{511keV,1} - \alpha_{511keV,2})/v_c. \quad (2)$$

We assume that the system is extended to be capable of triple-coincidence detection and reports additionally i_γ and

$$\begin{aligned} \Delta t_\gamma &= (t_{511keV,1} + t_{511keV,2})/2 - t_\gamma \\ &= \tau + (\alpha_{511keV,1} + \alpha_{511keV,2} - 2\alpha_\gamma)/(2v_c). \end{aligned} \quad (3)$$

Note that $\alpha_{511keV,1} + \alpha_{511keV,2}$ can be determined from the locations of detectors $i_{511keV,1}$ and $i_{511keV,2}$. Additionally, if Δt_{511keV} is precisely known, \mathbf{r}_{decay} can be identified, and then α_γ can be computed from i_γ and \mathbf{r}_{decay} . Then, Eq. (3) can be used to compute τ from Δt_γ .

In a real system, time measurement has limited precision and is typically binned and stored as integers. CRT refers to the uncertainty of Δt_{511keV} in FWHM. With a finite CRT, \mathbf{r}_{decay} cannot be precisely determined. A CRT of 200 ps to 600 ps translates to an uncertainty of 3 cm to 9 cm in \mathbf{r}_{decay} . Similarly, Δt_γ will have limited precision and be binned. Hence, in Eq. (3) α_γ is not precisely observed and all the time measurements involved contain statistical variations.

B. Probability model for the TOF-PET PLI list-mode data

In conventional PET, data is associated with a line of response (LOR) $\mathcal{L}(i_{511keV,1}, i_{511keV,2})$ connecting two detectors $i_{511keV,1}$ and $i_{511keV,2}$ that capture the annihilation photons. In TOF-PET, an LOR is further segmented into a number of non-overlapping segments referred to as lines of segment (LOS), using a TOF binsize that equals to CRT/2. Each LOS is identified by a multi-index $c = (i_{511keV,1}, i_{511keV,2}, m)$, indicating the specific TOF bin m on the LOR. We assume that the PLI events are given by $w = (c, i_\gamma, \Delta t_\gamma)$, where c identifies the LOS, i_γ is the detector that captures the prompt gamma, and Δt_γ is the time difference between the detection of the annihilation photons and the prompt gamma. These PLI events are stored as list-mode (LM) data, represented as $\mathcal{W}_{N_k} = \{w_k\}_{k=1}^{N_k}$, where k indexes a list of event words $w_k = (c_k, i_{\gamma,k}, \Delta t_{\gamma,k})$ and N_k is the total number of events.

1) *Calculation of the system matrix:* Each element $H_{c,j}$ of the system matrix \mathbf{H} is designed to reflect the likelihood that an annihilation taking place in image pixel j results in a detection at LOS c . The system matrix is calculated using a ray-tracing method [25], [26], identifying which pixels are intersected by $\mathcal{L}(i_{511keV,1}, i_{511keV,2})$ and the boundary points of intersection. A Gaussian function, whose width is given by the CRT, is placed along $\mathcal{L}(i_{511keV,1}, i_{511keV,2})$ and centered at the midpoint of these boundaries for each intersecting pixel j' . The integral of this Gaussian over each TOF bin yields the values for $H_{(i_{511keV,1}, i_{511keV,2}, m), j'}$, using $(2/\sqrt{\pi}) \int_a^b e^{-t^2} dt = \text{erf}(b) - \text{erf}(a)$, where $\text{erf}(x)$ is the error function. Pixels not intersected by the LOS are assigned a zero value in the system matrix.

¹Na-22 is a notable exception. See [20].

2) *Maximum likelihood estimation:* Let the vectors $\mathbf{f} = [f_j]$ and $\boldsymbol{\lambda} = [\lambda_j]$ be, respectively, the activity and o-P rate-constant images, where $f_j \geq 0$ and $\lambda_j \geq 0$ are their respective values in voxel j . τ_k can be computed from c_k , $i_{\gamma,k}$, and $\Delta t_{\gamma,k}$ to produce the LM data set $\mathcal{W}_{N_k}^0 = \{w_k^0\}_{k=1}^{N_k}$ with $w_k^0 = (c_k, \tau_k)$ in place of \mathcal{W}_{N_k} . We will derive in the Appendix that the log-likelihood for $\boldsymbol{\lambda}$ given \mathbf{f} and $\mathcal{W}_{N_k}^0$ is

$$\ell(\boldsymbol{\lambda}; \mathbf{f}, \mathcal{W}_{N_k}^0) = \sum_{k=1}^{N_k} \log \left(\sum_{j=1}^{N_j} H_{c_k, j} f_j \text{EMG}(\tau_k; \lambda_j, \sigma^2) \right), \quad (4)$$

where $\text{EMG}(\tau; \lambda, \sigma^2)$, the exponentially modified Gaussian (EMG) distribution, is the convolution of $\text{Exp}(\tau; \lambda)$ with a zero-mean Gaussian with standard deviation σ that is introduced to take in account the uncertainty in measurement of τ . The convolution can be explicitly evaluated to yield [27]:

$$\text{EMG}(\tau; \lambda, \sigma^2) = \frac{1}{2} \lambda e^{-\lambda(\tau - \frac{1}{2}\sigma^2\lambda)} \left(1 + \text{erf} \left(\frac{\tau - \lambda\sigma^2}{\sqrt{2}\sigma} \right) \right), \quad (5)$$

where $\text{erf}(x)$ is the error function. It can be checked that $\text{EMG}(\tau; \lambda, 0) = \text{Exp}(\tau; \lambda)$

Note that the TOF-PET PLI LM data contains the traditional TOF-PET LM data $\mathcal{C}_{N_k} = \{c_k\}_{k=1}^{N_k}$. Approaches for solving \mathbf{f} from \mathcal{C}_{N_k} , and from histogram-mode data derived from it, are well established [28]. A popular algorithm is the ordered-subsets (OS) expectation-maximization (EM) algorithm [29] that is an accelerated version of the EM algorithm for PET image reconstruction that can produce ML estimation (MLE) for \mathbf{f} . In this paper, we will employ the OS-EM algorithm for estimation of \mathbf{f} . The MLE of $\boldsymbol{\lambda}$ is then obtained by maximizing $\ell(\boldsymbol{\lambda}; \mathbf{f}, \mathcal{W}_{N_k}^0)$ given in Eq. (4) by using either the true \mathbf{f} or its estimate $\hat{\mathbf{f}}$ obtained by OS-EM. Maximization is carried out by using the Limited-memory Broyden-Fletcher-Goldfarb-Shanno Bound (L-BFGS-B) method available from `scipy.optimize` [19]. Positivity condition on $\boldsymbol{\lambda}$ is implemented but no explicit noise regularization schemes are introduced.

III. COMPUTER-SIMULATION STUDIES

A. Data generation

We generated the TOF-PET PLI LM data, \mathcal{W}_{N_k} , using Monte Carlo methods tailored for a scanner configuration with N_{det} detectors uniformly distributed on a diameter D . Given \mathbf{f} and $\boldsymbol{\lambda}$, we simulated the decay process as follows.

First, given a desired number of total decays, the image \mathbf{f} was scaled such that its pixel values represented the desired mean number of decays. Then, a list of decays was sampled from a Poisson distribution defined by these means. For each decay, its position, $\mathbf{r}_{decay} = (x_{decay}, y_{decay})^T$, was sampled within the bounds of the pixel area $A_j = [x_j - \Delta x/2, x_j + \Delta x/2] \times [y_j - \Delta y/2, y_j + \Delta y/2]$, where (x_j, y_j) represented the center coordinates of pixel j , and Δx and Δy were the pixel dimensions along the x and y axes, respectively, according to a uniform distribution, \mathcal{U}_{A_j} .

Then, a prompt gamma emitted in a random angle ϕ_γ , sampled from $\mathcal{U}[0, 2\pi)$, was generated at \mathbf{r}_{decay} . The travel distance α_γ before detection was determined by solving:

$$|\mathbf{r}_{decay} + \alpha_\gamma \hat{\boldsymbol{\phi}}_\gamma| = D/2, \quad (6)$$

where $\hat{\boldsymbol{\phi}} = (\cos \phi, \sin \phi)^T$ is the unit direction vector. This equation has two solutions given by

$$\alpha_\gamma^\pm = -\hat{\boldsymbol{\phi}}_\gamma^T \mathbf{r}_{decay} \pm \sqrt{(\hat{\boldsymbol{\phi}}_\gamma^T \mathbf{r}_{decay})^2 - \|\mathbf{r}_{decay}\|^2 + D^2/4}, \quad (7)$$

due to uniform sampling of ϕ_γ the solution α_γ^+ can be arbitrarily used for consistency, yielding $\mathbf{r}_{detect, \gamma} = \mathbf{r}_{decay} + \alpha_\gamma^+ \hat{\boldsymbol{\phi}}_\gamma$. The index i_γ of the detector that the prompt gamma hits was calculated by:

$$i_\gamma = \left\lfloor \left(\frac{N_{det}}{2\pi} \right) \angle \mathbf{r}_{detect, \gamma} \right\rfloor, \quad (8)$$

where $\angle \mathbf{r}$ denotes the angle of vector \mathbf{r} in polar coordinates, and $\lfloor x \rfloor$ represents the floor function.

Similarly, two opposing annihilation photons were emitted at \mathbf{r}_{decay} in a random angle ϕ_{511keV} sampled from $\mathcal{U}[0, 2\pi)$. The events were assumed to occur after an elapsed time drawn from an appropriate distribution. When only the o-Ps population was considered, this distribution was a single exponential distribution with a rate constant λ_j defined for pixel j . When two populations were considered, the distribution was a weighted mixture of two exponential distributions, each with its own rate constant defined for pixel j (see Sect. III-D). The distances $\alpha_{511keV,1}$ and $\alpha_{511keV,2}$, and detector indices $i_{511keV,1}$ and $i_{511keV,2}$ were calculated as described above, now using both solutions in Eq. (7). The emission angles ϕ_γ and ϕ_{511keV} were independent. The detection time $t_{511keV,1}$, $t_{511keV,2}$, and t_γ relative to the decay time t_{decay} were readily calculated from their travel distances divided by v_c , and the elapse time between positron annihilation and isotope decay.

To account for uncertainty in time measurement, every detection time was perturbed by a random number drawn from a Gaussian distribution having zero mean and standard deviation (SD) σ_1 . By convention, the CRT of the a TOF-PET system is the FWHM uncertainty in the coincidence time measurement. Therefore, $\sigma_1 = (\text{CRT}/2\sqrt{2\ln 2})/\sqrt{2}$. The TOF was then calculated using $\Delta t_{511keV} = t_{511keV,1} - t_{511keV,2}$, and

$$\Delta t_\gamma = (t_{511keV,1} + t_{511keV,2})/2 - t_\gamma. \quad (9)$$

The measured τ should be computed from Δt_γ by correcting for the travel-time difference between the prompt gamma and annihilation photons. This travel time difference can be estimated from $i_{511keV,1}$, $i_{511keV,2}$, i_γ , and Δt_{511keV} . For simplicity, in this work we used the exactly known travel distances and computed τ as:

$$\tau = \Delta t_\gamma - \frac{\alpha_{511keV,1} + \alpha_{511keV,2} - 2\alpha_\gamma}{2v_c}. \quad (10)$$

We generated TOF-PET PLI LM data with $N_{det} = 364$, $D = 57.2$ cm, and a specified CRT. Two numerical phantoms were considered, each consisting of an activity image and a rate-constant image. The activity and rate-constant images of Phantom 1 in Fig. 2 both contain four discs (radii = 12mm) on top of a circular background. In terms of pixel index, the centers of the upper left, upper right, lower left and lower right discs are at (13.5,14.5), (28.5,14.5), (13.5,27.5), and (28.5, 27.5) respectively. For the activity image, the disc-to-background ratio is 2:1. For the rate-constant image, the four discs have different λ values (0.2, 0.4, 0.6, and 0.8 ns⁻¹) and

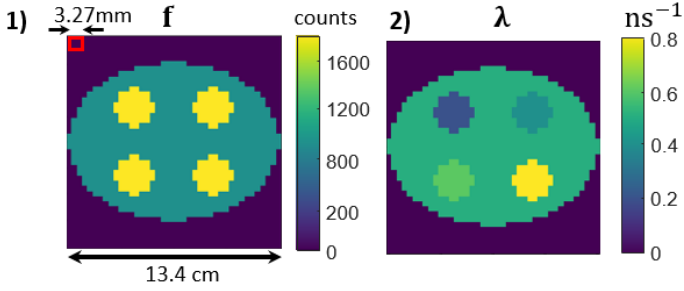


Fig. 2: (1) The activity image and (2) the rate-constant image of Phantom 1. These images consists of 3.27×3.27 mm² square pixels. Radius of each disc is 12 mm.

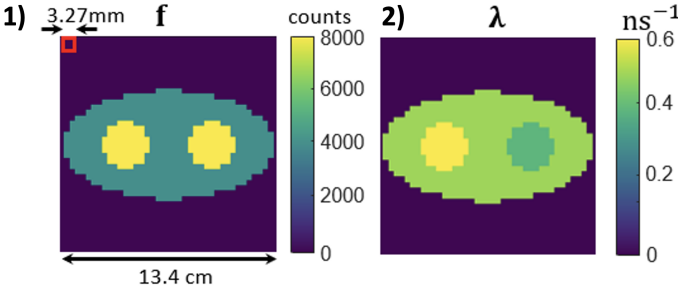


Fig. 3: (1) The activity image and (2) the rate-constant image of Phantom 2, with a pixel size of 3.27 mm. This phantom was used to examine the reconstruction method under different CRTs.

the background value is 0.5 ns^{-1} . Phantom 2 shown in Fig. 3 was considered for examining the effects of CRT. Its activity and rate-constant images feature an elliptical background enclosing two discs. In Phantom 2, the activity ratio is also 2:1. The decay-rate image for o-Ps includes two discs with different decay constants, λ (0.4 and 0.6 ns^{-1}), in contrast to the background ellipse with $\lambda = 0.5 \text{ ns}^{-1}$. Both phantoms contained 41×41 square pixels measuring 3.27×3.27 mm².

Unless mentioned otherwise, the expected total number of events to generate in each simulation run was one million. Our simulations considered only valid triple-coincidence events; attenuation, scattering, and random events were not included.

B. PLI reconstruction

1) *EMG/EXP-MLE methods*: Below, the proposed PLI reconstruction method is referred to as EMG-MLE. When estimating τ using Eq. (10), the variance in τ equals to the variance in Δt_γ , which, according to Eq. (9), is given by $(3/2)\sigma_1^2$. Therefore, the σ parameter in the EMG model was set to $\sqrt{3/2}\sigma_1 = (\sqrt{3}/2)(\text{CRT}/2.35)$. We may also set $\sigma = 0$. In this case, the EMG distribution reduces to the Exp distribution. For distinction, reconstruction using $\sigma = 0$ is referred to as Exp-MLE.

2) *The reference method*: The penalized surrogate (PS) method developed by Qi and Huang [14] was considered for comparison. This method updates an estimate for λ by:

$$\hat{\lambda}_j^{(m+1)} = \frac{\sum_{k=1}^{N_k} u_{c_k,j}^{(m)}}{\beta_j^m + \sum_{k=1}^{N_k} u_{c_k,j}^{(m)} \tau_k}, \quad (11)$$

where m is the iteration number,

$$u_{c_k,j}^{(m+1)} = \frac{H_{c_k,j} \hat{f}_j \lambda_j^{(m)} \exp(-\tau_k \times \lambda_j^{(m)})}{\sum_{l=1}^{N_j} H_{c_k,l} \hat{f}_l \lambda_l^{(m)} \exp(-\tau_k \times \lambda_l^{(m)})}, \quad (12)$$

and $\beta_j^m = \eta_j^m \beta$ where $\beta \geq 0$ is a regularization parameter and η_j^m is calculated from neighbors of pixel j to adjust the strength of regularization locally.

3) *Initial estimate and selection criterion*: As already mentioned above, either the known activity image \mathbf{f} or an estimate obtained from the simulated data using the OS-EM algorithm was used in the EMG/EXP-MLE and PS methods. The initial estimate for $\hat{\lambda}$ was a uniform image of 0.5 ns^{-1} . Given an image \mathbf{x} , the standardized absolute log ratio (SALR) is defined as [30]:

$$\text{SALR}(\mathbf{x})_p = \frac{|\log(\mathbf{x}_p/\mathbf{x}_b)|}{\text{SD}(\mathbf{x}_b)/\bar{\mathbf{x}}_b}, \quad (13)$$

where $\bar{\mathbf{x}}$ and $\text{SD}(\mathbf{x})$ are the average and standard deviation over pixels in \mathbf{x} , \mathbf{x}_p contains pixels of \mathbf{x} in a region of interest (ROI) p , and \mathbf{x}_b contains pixels of \mathbf{x} in the surrounding background of the ROI. As detailed in [30], higher SALR values are desired because it measures the contrast of an ROI against the background variability due to noise. Therefore, unless mentioned otherwise, for EMG-MLE, Exp-MLE and PS we calculate an overall SALR by averaging $\text{SALR}(\hat{\lambda})_p$, where p indexes the disc in the phantom, and select the iteration number that yields the largest overall SALR. All algorithms were run with a sufficiently large number of iterations so that the iteration yielding the max SALR could be identified.

C. Evaluation

For quantitative evaluation, we considered the normalized mean square error (NMSE), defined as:

$$\text{NMSE} = \frac{\|\hat{\lambda} - \lambda\|^2}{\|\lambda\|^2}, \quad (14)$$

where $\|\cdot\|$ denotes the Euclidean norm. We computed pixel-wise means and standard deviations of the NMSE of the images reconstructed from ten independent simulations, using EMG-MLE, Exp-MLE, and PS with $\beta = 0, 5, 10$. Then we obtained the average mean and standard deviation inside various regions, including the four discs and the background circle excluding the discs.

We also conduct cross-correlation analysis to quantify potential cross-talk between the activity map used and the resulting $\hat{\lambda}$. The cross-correlation is defined as:

$$C := \frac{(\hat{\lambda} - \lambda)^T \cdot \mathbf{f}}{\|\lambda\| \|\mathbf{f}\|}. \quad (15)$$

D. Initial examination of multi-population PLI reconstruction

So far, we have considered the presence of only o-Ps. As already mentioned, substantially faster DA and p-P populations co-exist, and proportions of the DA, p-P and o-P populations, approximately equal to 0.6, 0.1, and 0.3, are not sensitive to the environment [11]. We extended our simulations to include two rate-constant images, λ_1 for o-P and λ_2 for DA,

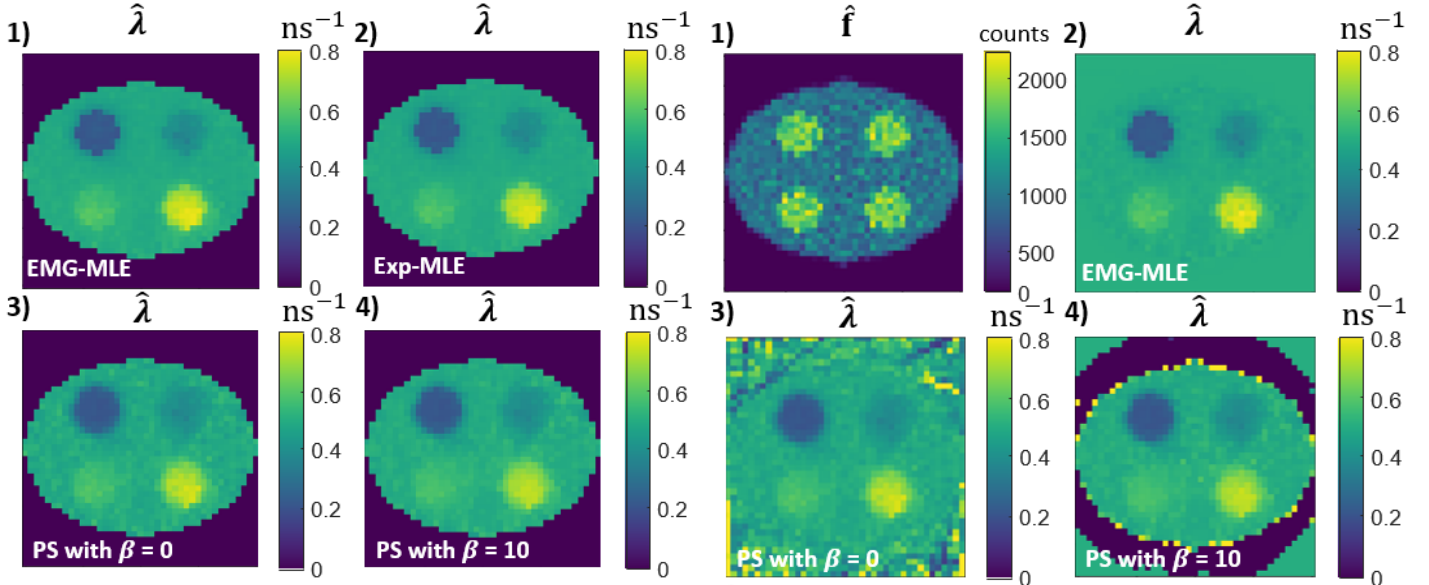


Fig. 4: Results obtained for Phantom 1 by using (1) the EMG-MLE method, (2) the Exp-MLE method, (3) the PS method [14] with $\beta = 0$, and (4) the PS method with $\beta = 10$. The true \mathbf{f} is used in these reconstructions.

neglecting the p-P population for now due to its relatively small population weight. As described in Appendix, in this case $\text{EMG}(\tau_k; \lambda_j, \sigma^2)$ in Eq. (4) will be replaced with

$$w_1 \text{EMG}(\tau_k; \lambda_{1,j}, \sigma^2) + w_2 \text{EMG}(\tau_k; \lambda_{2,j}, \sigma^2), \quad (16)$$

where $\lambda_{1,j}$ and $\lambda_{2,j}$ are the values of λ_1 and λ_2 at pixel j , respectively, and w_1 and w_2 with $w_1 + w_2 = 1$ are the population weights for o-P and DA events, respectively. The isotope image \mathbf{f} and the o-P rate-constant image λ_1 remained those of Phantom 2. On the other hand, the DA rate-constant image λ_2 was the background ellipse of the phantom taking the value of 2.5 ns^{-1} . Also, $w_1 = 0.3$ was used. The number of PLI events produced in a simulation run was again one million. In reconstruction, the exactly known w_1 , λ_2 and \mathbf{f} were used for obtaining the MLE of λ_1 . More details about the two-population model can be found in [30].

IV. RESULTS

A. Rate-constant image reconstruction

We considered a CRT of 400 ps and, as described above, 200 ps-width TOF bins. These settings resulted in 2.52 million TOF-PET channels. Fig. 4 illustrates the outcomes of various reconstruction methods applied to Phantom 1. Fig. 4(1) & 4(2) show the rate-constant images, $\hat{\lambda}_{\text{EMG-MLE}}$ and $\hat{\lambda}_{\text{Exp-MLE}}$, obtained by EMG-MLE and Exp-MLE, respectively. Fig. 4(3) & 4(4) show the results of the PS method by using $\beta = 0$ and 10, respectively. These results were obtained by using the true activity image \mathbf{f} and setting pixel values outside the phantom to zero. Subjectively, the PS image using $\beta = 0$ exhibits slightly larger background variability, but overall the differences between these images are not readily apparent.

Fig. 5 compares the rate-constant images obtained when using $\hat{\mathbf{f}}$ produced from the simulated data using the OS-EM

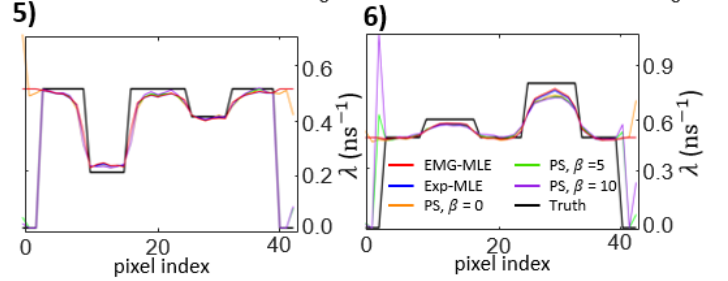


Fig. 5: Results obtained for Phantom 1. $\hat{\mathbf{f}}$ in panel (1) shows the activity image reconstructed from simulated data using OS-EM. $\hat{\lambda}$ in panels 2), 3), and 4) are rate-constant images obtained by, respectively, EMG-MLE, PS with $\beta = 0$, and PS with $\beta = 10$ when using $\hat{\mathbf{f}}$. Plots in panels 5) & 6) show horizontal profiles across the center of, respectively, the upper and lower discs of these rate-constant images. For comparison, the true profiles and the profiles of rate-constant images obtained by Exp-MLE and PS with $\beta = 5$, using $\hat{\mathbf{f}}$, are also shown.

algorithm. With $\hat{\mathbf{f}}$ and without setting the background outside the oval region as zero, although the activity is low in the area external to the phantom, it does not vanish. The EMG-MLE image shown in Fig. 5(2) did not apply constraints to updating pixels outside the phantom. This indicates that the observed stable pixel values are not due to any special regularization in these external regions, where the estimated activity image value remains low. As a result, unlike those shown in Fig. 4, the values of the pixels external to the phantom remained close to their initial values, which is equal to the background circle (0.5 ns^{-1}). In PS, significant streaks occur when using $\beta = 0$ (no regularization) and they can be removed when using $\beta = 10$. Based on the profiles in Fig. 5(5) & 5(6), the upper discs of the EMG-MLE are comparable with, while the lower discs are closer to the true values than, those in the PS images.

Fig. 6 show the NMSE results obtained for various reconstruction methods when using estimated $\hat{\mathbf{f}}$. They demonstrate that EMG-MLE can achieve lower NMSE means, or at least

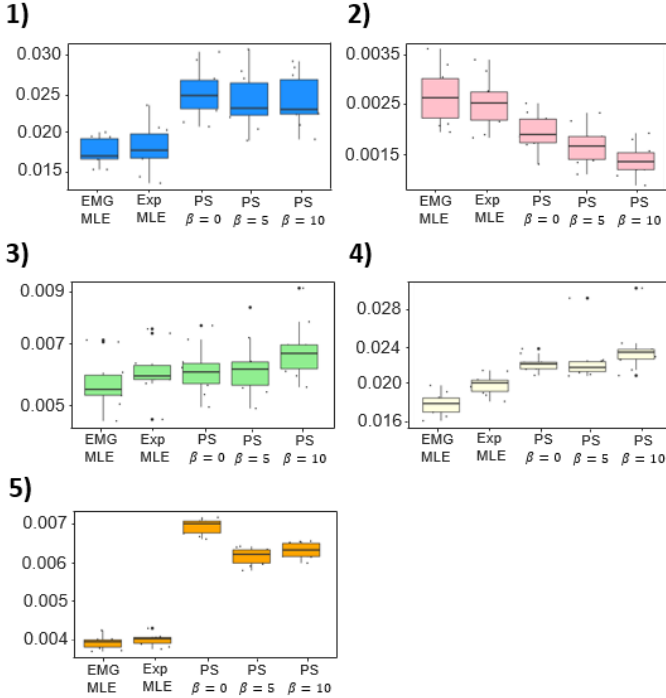


Fig. 6: Boxplots of NMSE of the EMG-MLE, Exp-MLE, and PS using $\beta = 0, 5, 10$ reconstructions of Phantom 1 in (1) upper-left disc, (2) upper-right disc, (3) lower-left disc, (4) lower-right disc, and (5) background disc, respectively. Simulated data contained one million events. Estimated \hat{f} was used in reconstruction.

comparable to those of PS, particularly for the upper-left disc, the lower-right disc, and the background disc. Most standard deviations given by EMG-MLE are lower than those by PS. Table S1 in the Supplementary data additionally compares the NMSE results for various reconstruction methods when using the true f and the estimated \hat{f} . Notably, when using the true f , EMG-MLE achieves only slightly lower average NMSE means and standard deviations than when using the estimated \hat{f} . This suggests stability of EMG-MLE with respect to noise even though no explicitly noise regularization scheme is incorporated.

Table I reports the cross-correlation values calculated by using Eq. (15). The low values indicate negligible interactions from f into $\hat{\lambda}$ for all methods examined.

These results underscore the efficacy of EMG-MLE in accurately reconstructing rate-constant images from TOF-PET data with a CRT of 400 ps.

B. The presence of an additional constant decay component

Fig. 7 shows the reconstructed o-P rate-constant image of the single-population and two-population model for Phantom 2, obtained from a single simulation, using one million events and 400 ps CRT. The reconstructed image of the two-population model yields a higher contrast of two circular regions relative to the background compared to the single-population model. In addition, the single-population model fails to reconstruct the difference in the rate-constant value between the two circular regions. This preliminary experiment

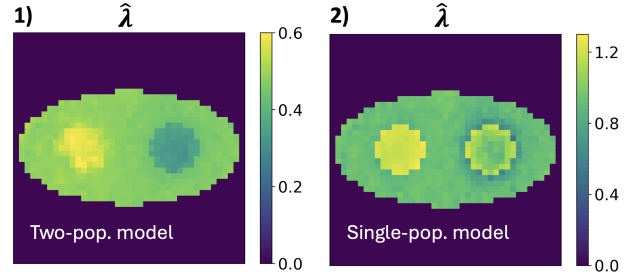


Fig. 7: o-P rate-constant image obtained for Phantom 2 from a single simulation data consisting of two event populations by using (1) the single-population method and (2) two-population model.

shows that the proposed method can be extended to handle multi-population data.

Table II presents the cross-correlation between the activity map and the reconstructed o-Ps rate-constant images. This comparison includes results from two scenarios: one using a two-population simulation with a two-component EMG likelihood estimate, and the other using two-population simulation but with a single-component EMG likelihood estimate. Both the two-population and single-population models show negligible interaction between f and $\hat{\lambda}$. Furthermore, the NMSE values of the reconstructed o-P rate-constant images for the three regions (left disc, right disc, and background) are summarized in Table S2 in the Supplementary data. The two-population model demonstrates significantly lower NMSE for all three regions compared to the single-population model.

V. SUMMARY AND DISCUSSIONS

In this study, we presented a probabilistic model for finding the ML solution of the positronium lifetime image from list-mode data acquired by a TOF-PET system that is extended for detecting triple coincidences when a $\beta^+\gamma$ isotope such as Sc-44 is used. We conducted computer simulation studies for a 2-D TOF-PET system that emulates the configurations of human TOF-PET systems with 288 detectors on a 57 cm diameter ring. CRTs of 200 ps, 400 ps, 600 ps, and 800 ps are considered for examining the effect of CRT on the resulting lifetime images.

Our results demonstrate that the estimated rate-constant images $\hat{\lambda}_{\text{EMG-MLE}}$ or $\hat{\lambda}_{\text{Exp-MLE}}$ agree well with the ground truth. The differences between Exp-MLE and PS with $\beta = 0$ shown in Fig. 6 may stem from the standardized absolute log ratio (SALR) stopping criterion, leading to relatively short iterations. As CRT increases, the accuracy of both methods generally decreases, but EMG-MLE consistently outperforms Exp-MLE. Our method incorporates Gaussian blur into the likelihood function and can be extended to a two-population model (o-P and p-P), which distinguishes it from existing approaches.

Our current studies have not accounted for attenuation, scatter, and random events. In addition, multiple lifetime populations are present and we have only preliminarily extended the proposed method to include two populations (direct annihilation of positron with electron also is characterized by its own

Cross-correlation					
Regions	EMG-MLE	Exp-MLE	PS $\beta = 0$	PS $\beta = 5$	PS $\beta = 10$
Upper left	1.20×10^{-1} (5.91×10^{-3})	1.23×10^{-1} (8.39×10^{-3})	1.43×10^{-1} (8.23×10^{-3})	1.41×10^{-1} (8.57×10^{-3})	1.41×10^{-1} (9.02×10^{-3})
Upper right	-6.14×10^{-4} (5.39×10^{-3})	2.64×10^{-3} (7.58×10^{-3})	1.11×10^{-2} (3.40×10^{-3})	9.45×10^{-3} (4.35×10^{-3})	8.13×10^{-3} (4.47×10^{-3})
Lower left	-6.72×10^{-2} (5.90×10^{-3})	-7.08×10^{-2} (5.94×10^{-3})	-7.09×10^{-2} (5.41×10^{-3})	-7.38×10^{-2} (6.36×10^{-3})	-7.78×10^{-2} (5.98×10^{-3})
Lower right	-1.20×10^{-1} (5.17×10^{-3})	-1.29×10^{-1} (4.07×10^{-3})	-1.41×10^{-1} (3.37×10^{-3})	-1.44×10^{-1} (8.49×10^{-3})	-1.49×10^{-1} (9.31×10^{-3})
Background	-2.73×10^{-2} (1.85×10^{-3})	-2.94×10^{-2} (1.62×10^{-3})	-3.21×10^{-2} (1.99×10^{-3})	-2.47×10^{-2} (1.90×10^{-3})	-1.53×10^{-2} (1.93×10^{-3})

TABLE I: Cross-correlations obtained for Phantom 1 using $\hat{\mathbf{f}}$. The SD is shown in the parenthesis.

decay rate constant). Moving forward, we plan to extend our model to include these factors to fit real-world PLI data more accurately. Triple coincidences have a much lower probability of occurrence than the conventional annihilation coincidences. Although emerging systems such as the Total-Body systems can offer an adequate sensitivity [31], we expect the PLI data to be count limited in general. Therefore, resolution-preserving noise regularization can be an important consideration in PLI reconstruction. Given the complexity, discrepancies between the model assumed for reconstruction and the data are very likely to exist. Another issue of practical significance is the computation complexity when extending the method to 3-D TOF-PET systems. Therefore, we also plan to delve into Bayesian modeling and regularized optimization, coupled with parallel computation strategies, to develop accurate, robust, and compute-efficient reconstruction algorithms for PLI.

APPENDIX

In this appendix, we elaborate on the derivation of the joint likelihood for the PLI data acquired by using a TOF-PET system. Let $f_j \geq 0$ be the PET activity in pixel j so that the number of positrons released in pixel j during an interval T is a Poisson random number with mean $f_j T$. A released positron in pixel j can exist for a duration whose distribution following an exponential distribution $\text{Exp}(\tau; \lambda_j)$ with some $\lambda_j \geq 0$ before annihilation. Assume that the uncertainty in the measurement of τ is described by $g(\tau; 0, \sigma^2)$ – a zero-mean Gaussian with standard deviation σ , the distribution of the observed τ will be the convolution of $\text{Exp}(\tau; \lambda)$ with $g(\tau; 0, \sigma^2)$, which can be evaluated to yield the Exponentially Modified Gaussian $\text{EMG}(\tau; \lambda_j, \sigma^2)$ given in Eq. (5). Subsequently, annihilation of a positron produces two opposite 511 keV photons that may be detected by the TOF-PET system at an LOS, say $c = (i_{511\text{keV},1}, i_{511\text{keV},2}, m)$ where $i_{511\text{keV},1}$ and $i_{511\text{keV},2}$ are the indices of the detectors making the detection and m is the TOF index (the TOF value is typically binned). In this treatment, a PLI detection is given by (c, τ) .

Let $\mathbf{f} = [f_j]^T$ and $\boldsymbol{\lambda} = [\lambda_j]^T$ be vectors representing the activity and rate-constant images. Given a PLI detection, we denote by $p(c, \tau | \boldsymbol{\lambda}, \mathbf{f}) d\tau$ the probability for it to be in the set $S_{d\tau}(c, \tau) = \{(c, \tau') : \tau \leq \tau' < \tau + d\tau\}$ when the activity and rate-constant image are \mathbf{f} and $\boldsymbol{\lambda}$, respectively. Evidently, $p(c, \tau | \boldsymbol{\lambda}, \mathbf{f}) d\tau$ equals to the ratio of $n_1(S_{d\tau}(c, \tau))$, the expected

number of detections in $S_{d\tau}(c, \tau)$, to n_2 , the expected total number of all detections. Evidently,

$$n_1(S_{d\tau}(c, \tau)) = \sum_{j=1}^{N_j} f_j T \times \text{EMG}(\tau; \lambda_j, \sigma^2) d\tau \times H_{c,j}, \quad (17)$$

where $f_j T$ gives the expected number of positrons in pixel j , $\text{EMG}(\tau; \lambda_j, \sigma^2) d\tau$ gives the probability for one of these positrons to exist for a duration $\tau' \in [\tau, \tau + d\tau]$, and $H_{c,j}$ gives the probability for an annihilation in pixel j to yield a detection at LOS c . Here we have made two assumptions: (i) the isotope decay, positron annihilation, and coincidence detection in a chain leading to a PLI detection are independent processes, and (ii) the processes involved in different PLI detections are independent. n_2 is the totality of $n_1(S_{d\tau}(c, \tau))$ over all possible c and τ :

$$n_2 = \sum_c \int_{\tau} S_{d\tau}(c, \tau) d\tau = T s_{\mathbf{f}}, \quad (18)$$

where $s_{\mathbf{f}} = \sum_{c,j} H_{c,j} f_j$. Therefore,

$$p(c, \tau | \boldsymbol{\lambda}, \mathbf{f}) = \frac{1}{d\tau} \frac{n_1}{n_2} = \frac{\sum_{j=1}^{N_j} H_{c,j} f_j \text{EMG}(\tau; \lambda_j, \sigma^2)}{s_{\mathbf{f}}}. \quad (19)$$

Note that $p(c, \tau | \boldsymbol{\lambda}, \mathbf{f})$ is a probability in c but a density in τ .

Under independence assumptions, given N_k detections the probability for them to be $(c_1, \tau_1), \dots, (c_{N_k}, \tau_{N_k})$ is therefore $p(\mathcal{W}_{N_k}^0; \boldsymbol{\lambda}, \mathbf{f}) = \prod_{k=1}^{N_k} p(c_k, \tau_k | \boldsymbol{\lambda}, \mathbf{f})$, where $\mathcal{W}_{N_k}^0 = \{(c_k, \tau_k) : 1 \leq k \leq N_k\}$. Consequently, we have the log-likelihood

$$\ell(\boldsymbol{\lambda}, \mathbf{f}; \mathcal{W}_{N_k}^0) = \sum_{k=1}^{N_k} \log \left(\sum_{j=1}^{N_j} H_{c_k,j} f_j \text{EMG}(\tau_k; \lambda_j, \sigma^2) \right) - N_k \log(s_{\mathbf{f}}). \quad (20)$$

Above we consider preset-count (PC) acquisition in which a scan is stopped when reaching a prescribed number N_k of detection. Alternatively, in preset-time (PT) acquisition a scan is conducted for a prescribed duration T and hence N_k becomes a Poisson random number with mean $n_2 = T s_{\mathbf{f}}$. With PT acquisition, the probability for having N_k detections and they are given by $\mathcal{W}_{N_k}^0$ is then $p'(\mathcal{W}_{N_k}^0; \boldsymbol{\lambda}, \mathbf{f}, T) = \text{Poisson}(N_k; T s_{\mathbf{f}}) \times p(\mathcal{W}_{N_k}^0; \boldsymbol{\lambda}, \mathbf{f})$, yielding the log-likelihood (omitting constants):

$$\ell'(\boldsymbol{\lambda}, \mathbf{f}; \mathcal{W}_{N_k}^0, T) = \sum_{k=1}^{N_k} \log \left(\sum_{j=1}^{N_j} H_{c_k,j} f_j \text{EMG}(\tau_k; \lambda_j, \sigma^2) \right) - T s_{\mathbf{f}}. \quad (21)$$

If \mathbf{f} is known *a priori*, the 2nd terms of these log-likelihoods are constants. Therefore, omitting constants both acquisition

Cross-correlation		
Regions	Two-population	Single-population
Left Disc	-1.15×10^{-3}	1.67×10^{-2}
Right Disc	-2.24×10^{-3}	-2.67×10^{-2}
Background	-1.06×10^{-4}	1.59×10^{-3}

TABLE II: Cross-correlations obtained for the single- and two-population method for Phantom 2 from a single simulation.

modes have the same profile log-likelihood given \mathbf{f} :

$$\ell(\boldsymbol{\lambda}; \mathcal{W}_{N_k}^0, \mathbf{f}) = \sum_{k=1}^{N_k} \log \left(\sum_{j=1}^{N_j} H_{c_k,j} f_j \text{EMG}(\tau_k; \lambda_j, \sigma^2) \right). \quad (22)$$

This profile likelihood function extends the model in [14] by replacing the exponential distribution with the exponentially modified Gaussian (EMG) distribution.

The gradient of $\ell(\boldsymbol{\lambda}; \mathcal{W}_{N_k}^0, \mathbf{f})$ is provided to the L-BFGS-B algorithm to speed up computation. It is an exercise to show

$$\frac{\partial \ell(\boldsymbol{\lambda}; \mathbf{f}; \mathcal{W}_{N_k}^0)}{\partial \lambda_j} = \sum_{k=1}^{N_k} \frac{H_{c_k,j} f_j \text{dEMG}(\tau_k; \lambda_j, \sigma^2)}{\sum_{j'=1}^{N_j} H_{c_k,j'} f_{j'} \text{EMG}(\tau_k; \lambda_{j'}, \sigma^2)}, \quad (23)$$

where

$$\begin{aligned} \text{dEMG}(\tau; \lambda, \sigma^2) &= \partial \text{EMG}(\tau; \lambda, \sigma^2) / \partial \lambda \\ &= \frac{1}{2} e^{-\lambda(\tau - \frac{1}{2}\sigma^2\lambda)} \left\{ -\frac{\sigma\lambda}{\sqrt{2\pi}} \exp^{-(\tau - \sigma^2\lambda)^2/2\sigma^2} \right. \\ &\quad \left. + (1 - \lambda\tau + \sigma^2\lambda^2) \left(1 + \text{erf} \left(\frac{\tau - \lambda\sigma^2}{\sqrt{2}\sigma} \right) \right) \right\}. \quad (24) \end{aligned}$$

As described in [2], positrons in fact can exist in multiple different states before annihilation, each of which is characterized by a distinct rate constant. In general, multiple rate-constant images, say $\boldsymbol{\lambda}_p$, $p = 1, \dots, N_p$, are therefore needed, and the probability distribution for the observed τ becomes $\sum_p w_p \text{EMG}(\tau; \lambda_{p,j}, \sigma^2)$ where w_p 's with $\sum_p w_p = 1$, $w_p \geq 0$ are the proportions of positrons existing in respective "populations" (we shall assume that the population weights do not vary over pixels) and $\lambda_{p,j}$ is the value of $\boldsymbol{\lambda}_p$ at pixel j . Following the above derivation, the profile log-likelihood given \mathbf{f} is

$$\begin{aligned} \ell(w_1, \boldsymbol{\lambda}_1, \dots, w_{N_p}, \boldsymbol{\lambda}_{N_p}; \mathcal{W}_{N_k}^0, \mathbf{f}) \\ = \sum_{k=1}^{N_k} \log \left(\sum_{j=1}^{N_j} H_{c_k,j} f_j \sum_{p=1}^{N_p} w_p \text{EMG}(\tau_k; \lambda_{p,j}, \sigma^2) \right). \quad (25) \end{aligned}$$

In Section III-D, we consider the case with $N_p = 2$ and treat w_1 , w_2 , and $\boldsymbol{\lambda}_2$ as constants, obtaining $\ell(\boldsymbol{\lambda}_1; w_1, w_2, \boldsymbol{\lambda}_2, \mathcal{W}_{N_k}^0, \mathbf{f})$. In this case, we need the gradient

$$\begin{aligned} \partial \ell(\boldsymbol{\lambda}_1; w_1, w_2, \boldsymbol{\lambda}_2, \mathcal{W}_{N_k}^0, \mathbf{f}) / \partial \lambda_{1,j} \\ = \sum_k \frac{H_{c_k,j} f_j w_1 \text{dEMG}(\tau_k; \lambda_{1,j}, \sigma^2)}{\sum_{j'} H_{c_k,j'} f_{j'} \sum_{p=1}^2 w_p \text{EMG}(\tau_k; \lambda_{p,j'}, \sigma^2)}. \quad (26) \end{aligned}$$

Although this paper does not consider the simultaneous MLE of \mathbf{f} and $\boldsymbol{\lambda}$ using the joint log-likelihoods, several observations are worth noting. First, from Eq. (20) it can be readily checked that $\ell(\boldsymbol{\lambda}, \boldsymbol{\xi}; \mathcal{W}_{N_k}^0) = \ell(\boldsymbol{\lambda}, \mathbf{f}; \mathcal{W}_{N_k}^0)$ for any $\boldsymbol{\xi} > 0$. This reflects that, since PC acquisition does not care about scan time, \mathbf{f} scanned for an interval ξT and $\boldsymbol{\xi} \mathbf{f}$ scanned for an interval T are equally likely to explain a given dataset.

This observation leads us to stipulate that the log-likelihood maximizing \mathbf{f} for PC- and PT-acquisitions differ only in scale. To verify this, using Eq. (20) & (21) we have

$$\ell'(\boldsymbol{\lambda}, \boldsymbol{\xi}; \mathcal{W}_{N_k}^0) = \ell(\boldsymbol{\lambda}, \mathbf{f}; \mathcal{W}_{N_k}^0) + \alpha(\mathbf{f}, \boldsymbol{\xi}), \quad (27)$$

where $\alpha(\mathbf{f}, \boldsymbol{\xi}) = N_k \log(s_{\mathbf{f}}) + N_k \log(\boldsymbol{\xi}) - \boldsymbol{\xi} T s_{\mathbf{f}}$. One can easily check that, for any \mathbf{f} , $\alpha(\mathbf{f}, \boldsymbol{\xi})$ can reach its maximum value of $N_k \log(N_k/eT)$ by setting $\boldsymbol{\xi} = N_k/T s_{\mathbf{f}}$. Therefore, if $(\mathbf{f}^*, \boldsymbol{\lambda}^*)$ maximizes $\ell(\boldsymbol{\lambda}, \mathbf{f}; \mathcal{W}_{N_k}^0)$, then $(\boldsymbol{\xi}^* \mathbf{f}^*, \boldsymbol{\lambda}^*)$, $\boldsymbol{\xi}^* = N_k/T s_{\mathbf{f}^*}$ maximizes $\ell'(\boldsymbol{\lambda}, \mathbf{f}; \mathcal{W}_{N_k}^0)$ because both terms on the right-hand side of Eq. (27) are maximized. Consequently, it is sufficient to consider only the PC joint log-likelihood $\ell(\boldsymbol{\lambda}, \mathbf{f}; \mathcal{W}_{N_k}^0)$. It is not difficult to see that the role of scaling by $\boldsymbol{\xi}^*$ is to fix the activity of a PC MLE solution to produce a PT MLE solution that best accounts for the observation of N_k events during the prescribed scan time T .

REFERENCES

- [1] P. Moskal, D. Kisielewska, C. Curceanu, E. Czerwiński, K. Dulski, A. Gajos, M. Gorgol, B. Hiesmayr, B. Jasińska, K. Kacprzak *et al.*, "Feasibility study of the positronium imaging with the J-PET tomograph," *Physics in Medicine & Biology*, vol. 64, no. 5, p. 055017, 2019.
- [2] P. Moskal, B. Jasińska, E. Stepień, and S. D. Bass, "Positronium in medicine and biology," *Nature Reviews Physics*, vol. 1, no. 9, pp. 527–529, 2019.
- [3] P. Moskal, D. Kisielewska, R. Y. Shopa, Z. Bura, J. Chhokar, C. Curceanu, E. Czerwiński, M. Dadgar, K. Dulski, J. Gajewski *et al.*, "Performance assessment of the 2 γ positronium imaging with the total-body PET scanners," *EJNMMI physics*, vol. 7, no. 1, pp. 1–16, 2020.
- [4] K. Shibuya, H. Saito, F. Nishikido, M. Takahashi, and T. Yamaya, "Oxygen sensing ability of positronium atom for tumor hypoxia imaging," *Communications Physics*, vol. 3, no. 1, p. 173, 2020.
- [5] B. Zgardzińska, G. Chołubek, B. Jarosz, K. Wysogład, M. Gorgol, M. Goździuk, M. Chołubek, and B. Jasińska, "Studies on healthy and neoplastic tissues using positron annihilation lifetime spectroscopy and focused histopathological imaging," *Scientific Reports*, vol. 10, no. 1, p. 11890, 2020.
- [6] M. D. Harpen, "Positronium: Review of symmetry, conserved quantities and decay for the radiological physicist," *Medical Physics*, vol. 31, no. 1, pp. 57–61, 2004.
- [7] P. Moskal and E. Stepień, "Positronium as a biomarker of hypoxia," *Bio-Algorithms and Med-Systems*, vol. 17, no. 4, pp. 311–319, 2021.
- [8] J. S. Karp, V. Viswanath, M. J. Geagan, G. Muehlechner, A. R. Pantel, M. J. Parma, A. E. Perkins, J. P. Schmall, M. E. Werner, and M. E. Daube-Witherspoon, "Pennpet explorer: design and preliminary performance of a whole-body imager," *Journal of Nuclear Medicine*, vol. 61, no. 1, pp. 136–143, 2020.
- [9] B. A. Spencer, E. Berg, J. P. Schmall, N. Omidvari, E. K. Leung, Y. G. Abdelhafez, S. Tang, Z. Deng, Y. Dong, Y. Lv *et al.*, "Performance evaluation of the uEXPLORER total-body PET/CT scanner based on NEMA NU 2-2018 with additional tests to characterize pet scanners with a long axial field of view," *Journal of Nuclear Medicine*, vol. 62, no. 6, pp. 861–870, 2021.
- [10] I. Alberts, J.-N. Hünermund, G. Prenosil, C. Mingels, K. P. Bohn, M. Viscione, H. Sari, B. Vollnberg, K. Shi, A. Afshar-Oromieh *et al.*, "Clinical performance of long axial field of view pet/ct: a head-to-head intra-individual comparison of the biograph vision quadra with the biograph vision pet/ct," *European journal of nuclear medicine and molecular imaging*, vol. 48, pp. 2395–2404, 2021.

- [11] P. Moskal, K. Dulski, N. Chug, C. Curceanu, E. Czerwiński, M. Dadgar, J. Gajewski, A. Gajos, G. Grudzień, B. C. Hiesmayr *et al.*, “Positronium imaging with the novel multiphoton PET scanner,” *Science advances*, vol. 7, no. 42, p. eabh4394, 2021.
- [12] P. Moskal, A. Gajos, M. Mohammed, J. Chhokar, N. Chug, C. Curceanu, E. Czerwiński, M. Dadgar, K. Dulski, M. Gorgol *et al.*, “Testing cpt symmetry in ortho-positronium decays with positronium annihilation tomography,” *Nature communications*, vol. 12, no. 1, p. 5658, 2021.
- [13] K. Shibuya, H. Saito, H. Tashima, and T. Yamaya, “Using inverse laplace transform in positronium lifetime imaging,” *Physics in Medicine & Biology*, vol. 67, no. 2, p. 025009, 2022.
- [14] J. Qi and B. Huang, “Positronium lifetime image reconstruction for TOF PET,” *IEEE transactions on medical imaging*, vol. 41, no. 10, pp. 2848–2855, 2022.
- [15] H.-H. Huang, Z. Zhu, S. Boopasiri, Z. Chen, S. Pang, and C.-M. Kao, “A statistical reconstruction algorithm for positronium lifetime imaging using time-of-flight positron emission tomography,” 2024. [Online]. Available: <https://arxiv.org/abs/2206.06463>
- [16] B. Huang, Z. Wang, X. Zeng, A. Goldan, and J. Qi, “High-resolution positronium lifetime imaging of extended heterogeneous biological samples,” in *2023 IEEE Nuclear Science Symposium, Medical Imaging Conference and International Symposium on Room-Temperature Semiconductor Detectors (NSS MIC RTSD)*. IEEE, 2023, pp. 1–1.
- [17] R. Y. Shopa and K. Dulski, “Positronium imaging in J-pet with an iterative activity reconstruction and a multi-stage fitting algorithm,” *Bio-Algorithms and Med-Systems*, vol. 19, no. 1, pp. 54–63, 2023.
- [18] Z. Chen, L. An, C.-M. Kao, and H.-H. Huang, “The properties of the positronium lifetime image reconstruction based on maximum likelihood estimation,” *Bio-Algorithms and Med-Systems*, vol. 19, no. 1, pp. 1–8, 2023.
- [19] P. Virtanen, R. Gommers, T. E. Oliphant, M. Haberland, T. Reddy, D. Cournapeau, E. Burovski, P. Peterson, W. Weckesser, J. Bright, S. J. van der Walt, M. Brett, J. Wilson, K. J. Millman, N. Mayorov, A. R. J. Nelson, E. Jones, R. Kern, E. Larson, C. J. Carey, Í. Polat, Y. Feng, E. W. Moore, J. VanderPlas, D. Laxalde, J. Perktold, R. Cimrman, I. Henriksen, E. A. Quintero, C. R. Harris, A. M. Archibald, A. H. Ribeiro, F. Pedregosa, P. van Mulbregt, and SciPy 1.0 Contributors, “SciPy 1.0: Fundamental Algorithms for Scientific Computing in Python,” *Nature Methods*, vol. 17, pp. 261–272, 2020.
- [20] L. Jødal, C. L. Loirec, and C. Champion, “Positron range in pet imaging: non-conventional isotopes,” *Physics in Medicine & Biology*, vol. 59, no. 23, p. 7419, nov 2014. [Online]. Available: <https://dx.doi.org/10.1088/0031-9155/59/23/7419>
- [21] T. Matulewicz, “Radioactive nuclei for β^+ γ PET and theranostics: selected candidates,” *Bio-Algorithms and Med-Systems*, vol. 17, no. 4, pp. 235–239, 2021.
- [22] J. Chojiński and M. Łyczko, “Prospects for the production of radioisotopes and radiobioconjugates for theranostics,” *Bio-Algorithms and Med-Systems*, vol. 17, no. 4, pp. 241–257, 2021.
- [23] S. Ferguson, H.-S. Jans, M. Wuest, T. Riauka, and F. Wuest, “Comparison of scandium-44 g with other pet radionuclides in pre-clinical pet phantom imaging,” *EJNMMI physics*, vol. 6, no. 1, pp. 1–14, 2019.
- [24] K. Shibuya, E. Yoshida, F. Nishikido, T. Suzuki, T. Tsuda, N. Inadama, T. Yamaya, and H. Murayama, “Annihilation photon acollinearity in pet: volunteer and phantom fdg studies,” *Physics in Medicine & Biology*, vol. 52, no. 17, p. 5249, 2007.
- [25] R. L. Siddon, “Fast calculation of the exact radiological path for a three-dimensional ct array,” *Medical physics*, vol. 12, no. 2, pp. 252–255, 1985.
- [26] Z. Zhu, H.-H. Huang, and S. Pang, “Photon allocation strategy in region-of-interest tomographic imaging,” *IEEE Transactions on Computational Imaging*, vol. 6, pp. 125–137, 2019.
- [27] E. Grushka, “Characterization of exponentially modified gaussian peaks in chromatography,” *Analytical chemistry*, vol. 44, no. 11, pp. 1733–1738, 1972.
- [28] R. M. Leahy and J. Qi, “Statistical approaches in quantitative positron emission tomography,” *Statistics and Computing*, vol. 10, pp. 147–165, 2000.
- [29] H. M. Hudson and R. S. Larkin, “Accelerated image reconstruction using ordered subsets of projection data,” *IEEE transactions on medical imaging*, vol. 13, no. 4, pp. 601–609, 1994.
- [30] Z. Chen, C.-M. Kao, H.-H. Huang, and L. An, “Enhanced positronium lifetime imaging through two-component reconstruction in time-of-flight positron emission tomography,” *Frontiers in Physics*, vol. 12, p. 1429344, 2024.
- [31] K. Parodi, T. Yamaya, and P. Moskal, “Experience and new prospects of PET imaging for ion beam therapy monitoring,” *Zeitschrift für Medizinische Physik*, vol. 33, no. 1, pp. 22–34, 2023.

Mean (Standard deviation) of NMSE from the 10 simulation replicates						
Given	Regions	Proposed method	Exp-MLE	PS $\beta = 0$	PS $\beta = 5$	PS $\beta = 10$
f	Upper left	1.88×10^{-2} (1.93×10^{-3})	1.88×10^{-2} (1.78×10^{-3})	2.86×10^{-2} (3.35×10^{-3})	2.64×10^{-2} (2.70×10^{-3})	2.56×10^{-2} (2.99×10^{-3})
	Upper right	1.93×10^{-3} (3.70×10^{-4})	1.79×10^{-3} (2.67×10^{-4})	1.93×10^{-3} (3.48×10^{-4})	1.64×10^{-3} (3.62×10^{-4})	1.30×10^{-3} (3.23×10^{-4})
	Lower left	5.43×10^{-3} (7.64×10^{-4})	6.15×10^{-3} (8.90×10^{-4})	6.32×10^{-3} (8.33×10^{-4})	6.40×10^{-3} (8.83×10^{-4})	6.99×10^{-3} (8.87×10^{-4})
	Lower right	1.61×10^{-2} (9.54×10^{-4})	1.86×10^{-2} (1.04×10^{-3})	2.31×10^{-2} (8.67×10^{-4})	2.27×10^{-2} (1.22×10^{-3})	2.34×10^{-2} (1.33×10^{-3})
	Background	2.99×10^{-3} (1.77×10^{-4})	3.09×10^{-3} (1.82×10^{-4})	6.60×10^{-3} (1.95×10^{-4})	5.66×10^{-3} (2.07×10^{-4})	5.62×10^{-3} (1.98×10^{-4})
\hat{f}	Upper left	1.75×10^{-2} (1.78×10^{-3})	1.80×10^{-2} (3.03×10^{-3})	2.52×10^{-2} (3.25×10^{-3})	2.42×10^{-2} (3.62×10^{-3})	2.42×10^{-2} (3.37×10^{-3})
	Upper right	2.59×10^{-3} (5.23×10^{-4})	2.43×10^{-3} (4.87×10^{-4})	1.88×10^{-3} (3.46×10^{-4})	1.62×10^{-3} (3.66×10^{-4})	1.33×10^{-3} (3.07×10^{-4})
	Lower left	5.78×10^{-3} (8.52×10^{-4})	6.18×10^{-3} (8.53×10^{-4})	6.20×10^{-3} (8.02×10^{-4})	6.30×10^{-3} (9.49×10^{-4})	6.88×10^{-3} (9.49×10^{-4})
	Lower right	1.79×10^{-2} (1.26×10^{-3})	2.01×10^{-2} (1.13×10^{-3})	2.25×10^{-2} (8.93×10^{-4})	2.28×10^{-2} (2.58×10^{-3})	2.40×10^{-2} (2.70×10^{-3})
	Background	3.55×10^{-3} (1.68×10^{-4})	3.63×10^{-3} (1.59×10^{-4})	6.70×10^{-3} (2.14×10^{-4})	5.89×10^{-3} (2.29×10^{-4})	6.05×10^{-3} (2.06×10^{-4})

TABLE S1: Comparisons of NMSE using the five methods for Phantom 1 with f and \hat{f} . NMSE measurements of reconstructed images were taken across various regions including the upper left, upper right, lower left, lower right discs, and the background area defined by an ellipse excluding the four discs.

NMSE from a single simulation		
Regions	Two-population	Single-population
Left Disc	7.13×10^{-3}	1.38
Right Disc	2.07×10^{-2}	2.71
Background	4.06×10^{-3}	0.66

TABLE S2: Comparisons of NMSE using the single- and two-population method for Phantom 2 from a single simulation.